Mechanisms for a PNA-Like Teleconnection Pattern in Response to the MJO

KYONG-HWAN SEO AND HYUN-JU LEE

Department of Atmospheric Sciences, Division of Earth Environmental System, Pusan National University, Busan, South Korea

(Manuscript received 29 November 2016, in final form 8 March 2017)

ABSTRACT

Kinematic mechanisms of the Pacific–North America (PNA)-like teleconnection pattern induced by the Madden–Julian oscillation (MJO) is examined using an atmospheric general circulation model (GCM) and a barotropic Rossby wave theory. Observation shows that a negative PNA-like teleconnection pattern emerges in response to MJO phase-2 forcing with enhanced (suppressed) convection located over the Indian (western Pacific) Ocean. The GCM simulations show that both forcing anomalies contribute to creating the PNA-like pattern. Indian Ocean forcing induces two major Rossby wave source (RWS) regions: a negative region around southern Asia and a positive region over the western North Pacific (WNP). The negative RWS to the north of the enhanced convection in the Indian Ocean arises from southerly MJO-induced divergent wind crossing the Asian jet. Unexpectedly, another significant RWS region develops over the WNP owing to refracted northerly divergent wind. A ray-tracing method demonstrates three different ways of wave propagation emanating from the RWS to the PNA region: 1) direct arclike propagation from the negative RWS to the PNA region occurs in the longest waves, 2) shorter waves are displaced first downstream by the jet waveguide effect and then emanate at the jet exit to the PNA region, and 3) waves with zonal wavenumbers 1 and 2 exhibit canonical wave propagation from the positive RWS at the jet exit to the PNA region.

On the other hand, the positive RWS induced by western Pacific forcing shows similar characteristics to feature 3 described above, with some relaxation such that much shorter waves also contribute to the formation of the southern cells.

1. Introduction

The Madden–Julian oscillation (MJO) is the most dominant physical mode in the tropics on intraseasonal time scales (Madden and Julian 1972). It affects global weather and climate such as the surface air temperature over the central and eastern North American continent and East Asia (e.g., Vecchi and Bond 2004; Lin and Brunet 2009; Zhou et al. 2012; Seo et al. 2016), precipitation in Canada (e.g., Lin et al. 2010) and East Asia (e.g., Jeong et al. 2008), and Arctic surface air temperature amplification (e.g., Yoo et al. 2012). Recently, Seo et al. (2016) revealed that tropical diabatic heating located over the Indian Ocean leads to surface air warming over East Asia through subsidence caused by local Hadley circulation and surface warming over North America and cooling over eastern Europe through meridional temperature advection due to poleward-propagating Rossby waves. It has been demonstrated that approximately 30% of the total variability of upper-level circulation on intraseasonal time scales is explained by MJO-induced teleconnection anomalies (Matthews et al. 2004; Seo and Son 2012). Among the teleconnection fields, the Pacific–North America (PNA; Wallace and Gutzler 1981) circulation pattern is the most dominant midlatitude low-frequency mode over the downstream region of MJO diabatic forcing.

Prevailing theories on growth and maintenance of the PNA pattern include 1) a direct linear circulation response to diabatic heating or topography through poleward-propagating Rossby waves (e.g., Hoskins and Karoly 1981; Seo and Son 2012; Seo et al. 2016), 2) atmospheric internal growth by barotropic instability due to a zonally asymmetric climatological mean flow (e.g., Simmons et al. 1983; Branstator 1990, 1992), and 3) growth arising from dynamical feedback by high-frequency synoptic eddies (SEs) (e.g., Lau 1988; Branstator 1992; Nakamura and Wallace 1993; Feldstein 2002; Franzke and Feldstein 2005; Jin et al. 2006a,b; Kug and Jin 2009; Zhou et al. 2017). A number of recent studies on the PNA mechanism are related to the latter two processes characterized by the internal atmospheric

Corresponding author: Kyong-Hwan Seo, khseo@pusan.ac.kr

DOI: 10.1175/JAS-D-16-0343.1

dynamics, where precursor disturbances or positive feedbacks between SEs and low-frequency modes (LF; PNA is an example) act to develop the PNA anomalies. For instance, a quadrupole circulation anomaly pattern over East Asia and the western Pacific is found to be an optimal preconditioning signal for later development of the PNA (Cash and Lee 2001), with this process explaining approximately 70% of the observed PNA events. The first two upstream PNA circulation centers located over the North Pacific are identified to be caused by barotropic energy conversion from the zonally asymmetric background flow or by stationary and high-frequency transient eddy forcing (Feldstein 2002; Mori and Watanabe 2008; Franzke et al. 2011). A two-way interaction between SE and LF flow acts to sustain and amplify the PNA pattern, where the eddy vorticity forcing feedbacks onto the LF flow, which, in turn, organizes the eddy vorticity forcing (e.g., Jin et al. 2006a,b). Synoptic-eddy vorticity flux is found to be directed to the left side of the LF flow, inducing the convergence (divergence) of vorticity in the area of LF cyclonic (anticyclonic) circulation anomalies and thus amplifying the LF mode (Kug and Jin 2009; Ren et al. 2009).

On the other hand, initial synoptic disturbances may interact with tropical heating-induced wave train, amplifying the PNA anomalies. A large amplitude negative (positive) PNA pattern in response to tropical convective heating is found to be preceded by the existence of synoptic transient eddies over the northeastern Pacific (eastern Asia) (Franzke et al. 2011). In particular, an initial upper-level cyclonic circulation anomaly centered over northeastern China bounded by anticyclonic circulation anomalies to its south and north interacts with the MJO phase-1 convection-induced Rossby wave and develops a large negative PNA amplitude in 7–10 days (Goss and Feldstein 2015). This implies that the strengthened subtropical Asian jet (so increased potential vorticity gradient across the jet) gives rise to an enhanced circulation response over the PNA region.

Apart from these internal dynamical processes or interaction mechanism between initial synoptic eddies and the tropical convection-forced wave train, a detailed dynamical or kinematic mechanism related to external forcing (i.e., growth due to a wave response to tropical convection) needs to be investigated. A previous study demonstrated that approximately 30% of all PNA events are explained by MJO convection (Mori and Watanabe 2008). Therefore, to identify a nearly pure circulation response to the MJO, we remove the most unstable normal mode in a dynamical core model and investigate the formation mechanism of wave source and PNA-like circulation cells. The characteristics of wave energy propagation for different zonal wavenumbers are examined. Although it could be easily expected that diabatic forcing over the tropical Pacific induces a PNA-like pattern, we demonstrate in this study that the LF pattern can be driven by tropical forcing over the Indian Ocean, which is located significantly upstream from the tropical Pacific. Three different pathways for affecting PNA cells by Indian Ocean forcing will be presented.

Waves propagating downstream to the PNA region emanate from a Rossby wave source (RWS), which is mainly caused by anomalous upper-level divergent flow generated near areas of tropical heating (Sardeshmukh and Hoskins 1988; Jin and Hoskins 1995). This anomalous wind induces advection of the climatological mean absolute vorticity and divergence of the anomalous flow at first order (e.g., Lin 2009; Seo and Son 2012). The anomalous advection and divergence terms related to the induced vorticity anomaly are generally of much smaller amplitude. In this study, details of the formation mechanism of the RWS are investigated, and barotropic Rossby wave theory and ray-tracing method are applied to derive the Rossby wave group velocity propagation. It will be shown that the PNA-like pattern is formed by a rather complex process through four different ways of Rossby wave propagation. The performance of simulating the PNA-like pattern is also investigated using the recent archives from atmospheric and coupled model simulations performed by Working Group on Numerical Experimentation (WGNE) and MJO Task Force (MJO-TF).

In section 2, data and diagnostic methods are presented. Section 3 shows the results for the circulation response to the MJO in observation and a dry general circulation model (GCM) simulation, formation mechanism of RWS, and characteristics of Rossby wave energy propagation through ray tracing. In addition, performance in reproducing the PNA-like teleconnection pattern in state-of-art GCMs and coupled models is briefly examined. Summary and discussions are presented in section 4, together with a schematic description of the relevant physical processes.

2. Data and methodology

Daily mean outgoing longwave radiation (OLR) data from the Advanced Very High Resolution Radiometer (AVHRR) operated by the National Oceanic and Atmospheric Administration (NOAA) is used to represent the tropical convective anomalies (Liebmann and Smith 1996). Various global variables on a 2.5° × 2.5° grid are obtained from the European Centre for Medium-Range Weather Forecasts interim reanalysis dataset

(ERA-Interim; Dee et al. 2011). Boreal wintertime [December–February (DJF)] for the period from 1979 to 2010 is considered. The anomaly field for each variable is calculated by removing first three harmonics of the annual cycle, and intraseasonal variability is derived by 20–90-day filtering using a Lanczos filter.

The 20-yr climate model simulations are derived from the MJO global model comparison project organized by the WGNE and the MJO-TF and GEWEX Atmospheric System Study (GASS). A total of 27 different simulations from 24 atmospheric GCM and atmosphere–ocean coupled models are archived.

To extract the MJO signal, an empirical orthogonal function (EOF) analysis is performed with the filtered OLR anomaly. Using the first two EOF modes, eight MJO phases are derived (Wheeler and Hendon 2004). Cases where the normalized PC amplitude (i.e., $\sqrt{\mathrm{PC1}^2 + \mathrm{PC2}^2}$) is greater than 1.5 are used for composite analysis. To check the statistical significance of a composite map, a Monte Carlo test is performed with 500 random resamplings of the data, where original time series are randomly shifted to the right or left with a circular structure kept for each simulation. This way maintains an autocorrelation structure of the time series. Another independent Monte Carlo test by applying a 2-week window as one event also produces identical results.

A primitive-equation model based on the dynamical core of the Geophysical Fluid Dynamics Laboratory (GFDL) atmospheric GCM (Gordon and Stern 1982) is used to simulate the circulation response to tropical forcing. The model has a rhomboidal 30 (R30) horizontal resolution and 20 equally spaced sigma levels from 0.975 to 0.025. External forcing that mimics the spatial pattern of the MJO phase 2 (i.e., enhanced convection over the central Indian Ocean and suppressed convection over the western Pacific) is added into the temperature tendency equation. The heating/cooling anomaly is turned smoothly on for the first 2 days and then kept constant until day 5. No forcing is given after day 5. The vertical heating structure is the same as Fig. 3 of Seo and Son (2012), which has a peak around 450 hPa. To maintain a climatological mean state similar to the original input, a forcing term in the tendency equation is applied during model integration. By doing so, the most unstable normal mode is effectively eliminated so that a nearly pure circulation response to external forcing is achieved. In addition, since the model response to tropical forcing is almost linear [as shown in Seo and Son (2012)], opposite diabatic forcing (i.e., phase 6) produces the same results with only a sign reversal.

To investigate the Rossby wave propagation to the extratropics, the RWS is first examined using the following linearized barotropic vorticity equation (Sardeshmukh and Hoskins 1988):

$$\frac{\partial \zeta'}{\partial t} = S' - \overline{\mathbf{v}}_\psi \cdot \nabla \zeta' - \mathbf{v}'_\psi \cdot \nabla \overline{\zeta} + F', \tag{1}$$

where the overbar represents the climatological mean and the prime the perturbation; ζ is the absolute vorticity; $\mathbf{v}_\psi$ is the rotational velocity vector; S' denotes the RWS; and F' is a frictional term, which is considered negligible. The second and third terms represent the vorticity generation due to rotational wind-related vorticity advection. These terms signify the Rossby wave propagation (as compared to the RWS), which contributes to making the vorticity cells over the PNA area. The perturbation RWS represents the terms related to the divergent wind component:

$$S' = -\overline{\zeta}\nabla \cdot \mathbf{v}'_\chi - \mathbf{v}'_\chi \cdot \nabla \overline{\zeta} - \zeta' \nabla \cdot \overline{\mathbf{v}}_\chi - \overline{\mathbf{v}}_\chi \cdot \nabla \zeta', \tag{2}$$

where $\mathbf{v}_\chi$ is divergent wind. The first and second terms on the right-hand side of Eq. (2) indicate the generation of wave vorticity due to divergence by anomalous divergent wind and advection of the climatological absolute vorticity by the divergent wind anomaly, respectively. The third and fourth terms are the vorticity generation term by convergence of climatological divergent flow and anomalous vorticity advection by climatological divergent wind, respectively. Generally, the RWS terms are not greater than the rotational component-related terms in the barotropic vorticity equation because the divergent wind is usually smaller than the rotational wind. However, when strong diabatic forcing takes place, the RWS becomes significant.

Next, ray tracing is performed to identify the evolution of the nondivergent barotropic Rossby wave activity. The dispersion relationship for the barotropic Rossby wave is $\omega = \overline{U}k - \beta_* k/K^2$, where $\overline{U}$ is the basic zonal wind, $\beta_* = \partial f/\partial y - \partial^2 \overline{U}/\partial y^2$ is the meridional gradient of the absolute vorticity (with $\beta = \partial f/\partial y$), and $K = \sqrt{k^2 + l^2}$ represents the total wavenumber with the zonal and meridional wavenumbers, k and l, respectively. Note that a basic flow is a climatological wintertime 200-hPa zonal wind. To describe the stationary Rossby wave, the case of $\omega = 0$ is considered. The zonal and meridional vectors of the group velocities are $c_{gx} = \partial\omega/\partial k = c + 2\beta_* k^2/K^4$ and $c_{gy} = \partial\omega/\partial l = 2\beta_* kl/K^4$, respectively, obtained by a partial derivative of the dispersion relationship with respect to k and l. These group velocities are converted to the ray path of the Rossby wave activity as $dx/dt = c_{gx}$ and $dy/dt = c_{gy}$, and the location of the ray is calculated using a fourth-order Runge–Kutta method (Press et al. 1992; Seo and Son 2012).

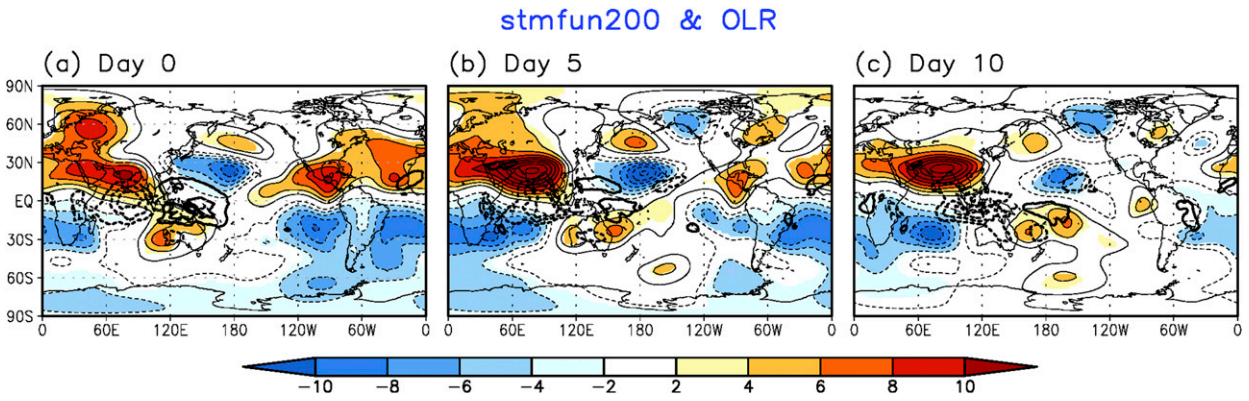

FIG. 1. Lagged composite maps of filtered 200-hPa streamfunction (shaded, intervals of 2.0×10^6 m^2 s^{-1}) and OLR (thick line, intervals of 10 W m^{-2}) anomalies at days (a) 0, (b) 5, and (c) 10 for initial MJO phase 2. Solid (dotted) lines indicate positive (negative) values. Shading indicates statistically significant regions at the 95% confidence level.

The significant RWS appearing on day 3 of model integration is used to seed the Rossby wave.

3. Results

a. *Circulation response to the MJO in observation and model simulation*

A lagged composite map of the 200-hPa streamfunction anomaly is presented in Fig. 1 with respect to MJO phase 2. Phase 2 corresponds to enhanced convection over the central Indian Ocean and suppressed convection over the western Pacific (thick black contour in Fig. 1a). Quadrupole circulation anomalies straddling the equator are observed in the subtropics of the Eastern Hemisphere, which have been identified as the combined effect of the equatorial Kelvin and Rossby waves by Seo and Son (2012). Over the North Pacific, dipole circulation anomalies appear with a cyclonic circulation anomaly that has the same center as one of the quadrupole subtropical circulation anomalies. As time progresses, MJO convection anomalies move eastward and a more complete circulation anomaly distribution exhibiting a negative PNA-like pattern emerges (Figs. 1b and 1c). Since the interval between two consecutive MJO phases is about 5–7 days, the composite maps of Figs. 1b and 1c coincide with MJO phases 3 and 4. Since the MJO largely exhibits an antisymmetric structure between the opposite phases, the result for the positive PNA-like pattern appearing at phases 7 or 8 is nearly the same with only a sign reversal (not shown).

The upper-troposphere streamfunction anomaly averaged over lag 5–10 days is plotted in Fig. 2a. The pattern correlation over the PNA region (0°–80°N, 140°E–60°W) between the circulation anomaly field at these lags and a typical PNA pattern obtained by regressing the reanalysis streamfunction data onto a daily PNA index provided by the NOAA Climate Prediction Center (CPC) (ftp://ftp.cpc.ncep.noaa.gov/cwlinks/) is 0.65. To reproduce the extratropical circulation anomalies, we added equatorial diabatic forcing, which mimics the observed convection anomalies of phase 2 (i.e., diabatic heating at 80°E and diabatic cooling at 150°E, as presented as thick solid and dotted contours, respectively, in Fig. 2b) to the temperature equation in the model. Figures 2c and 2d show the circulation response to each diabatic forcing at integration day 15. Interestingly, both responses result in the PNA-like pattern, suggesting that both enhanced and suppressed convections contribute to the combined circulation pattern shown in Fig. 2b. Because the model response to tropical forcing is nearly linear (Seo and Son 2012), the summation of both circulation responses is almost the same as the circulation field of Fig. 2b. A cyclonic circulation anomaly over the North Pacific (at 30°N) induced by enhanced convection at 80°E is slightly stronger than that caused by suppressed convection at 150°E. This is an interesting feature since the positive forcing anomaly is located far upstream, while the suppressed convection is located much closer to the North Pacific. However, if a Northern Hemispheric–mean streamfunction is removed, this cyclonic anomaly in response to western Pacific forcing becomes stronger than that induced by Indian Ocean heating (not shown). Almost identical features are found in the observation using a regression analysis with respect to OLR indices measured at 0°, 80°E and 0°, 150°E (not shown).

We investigate which forcing location is most effective for the generation of the PNA-like teleconnection pattern shown in Fig. 2b. To test this using the GCM, diabatic heating is forced at varying longitudes ranging from 30°E to 60°W at intervals of 10° along the equator and the pattern correlation of the induced circulation anomalies with respect to the negative PNA-like teleconnection pattern (Fig. 2b) is calculated for the Northern

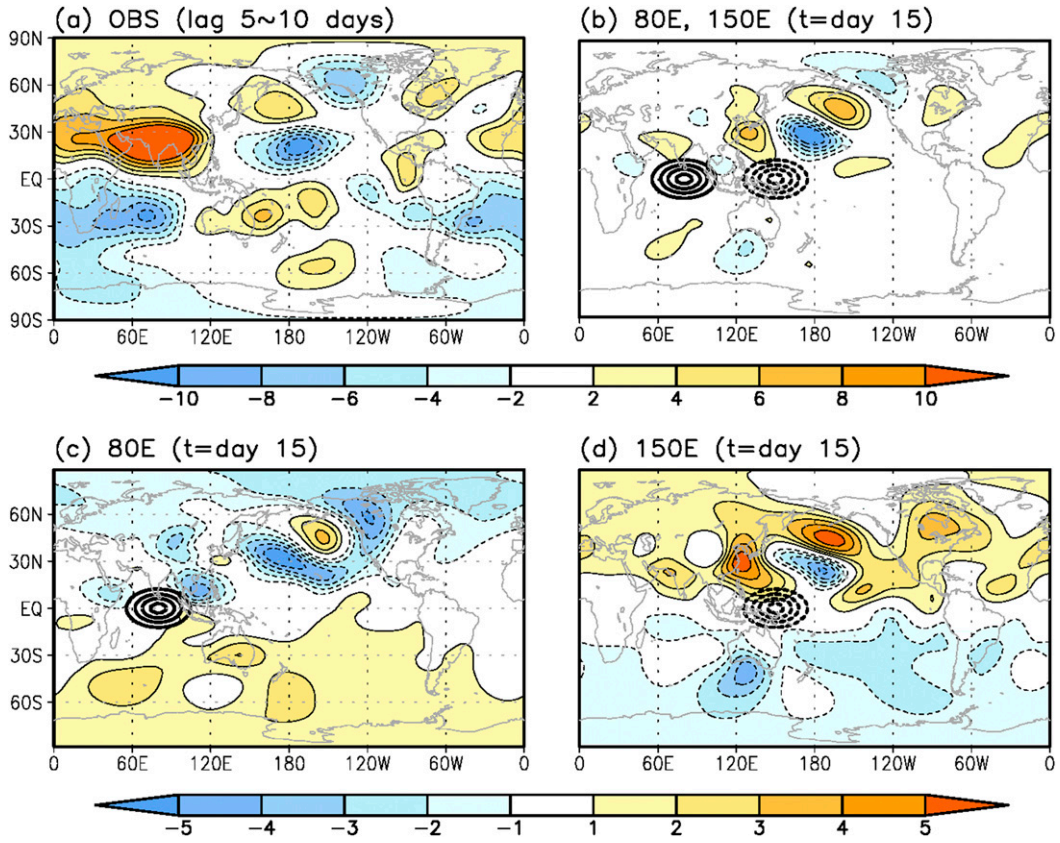

FIG. 2. (a) Composite map of 200-hPa streamfunction averaged over lag 5–10 days and (b) upper-troposphere ($\sigma = 0.225$) streamfunction anomaly at day 15 of the model simulation in response to diabatic heating at 80°E and diabatic cooling at 150°E. (c),(d) As in (b), but for a monopole forcing at 80° and at 150°E, respectively. The intervals of the streamfunction anomalies are $2.0 \times 10^6\,\mathrm{m^2\,s^{-1}}$ for (a) and (b) and $1.0 \times 10^6\,\mathrm{m^2\,s^{-1}}$ for (c) and (d). The thick solid (dotted) circles in (b)–(d) indicate diabatic heating (cooling) with intervals of $0.5\,\mathrm{K\,day^{-1}}$.

Hemisphere (NH) as a function of the integration time. Figure 3 shows that when diabatic heating is located at 60°–90°E, the most similar circulation response in the PNA region occurs after day 10. Similarly, diabatic heating placed in the longitudinal range of 130°–165°E induces the positive PNA-like pattern after day 10. These locations correspond exactly to phase-2 (or phase 3 to a lesser degree) initial forcing with enhanced convection over the Indian Ocean and suppressed convection over the far western Pacific. Therefore, this MJO phase 2 or nearby forcing is most effective for generating the negative PNA-like teleconnection pattern (Mori and Watanabe 2008; Franzke et al. 2011; Seo et al. 2016). Similarly, initial MJO phase 6 or 7 is most effective for producing the positive PNA-like pattern (not shown).

b. The Rossby wave source

To understand the dynamical mechanisms for the circulation response to forcing, the RWS calculated at day 3 of the model simulation is presented in Fig. 4. An exponential spectral filter of the form $\exp\{-K[n(n+1)]^2\}$ is used to smooth RWS fields as shown in Sardeshmukh and Hoskins (1984) and Seo and Son (2012), where K is chosen such that the highest wavenumber spectral coefficients are multiplied by 0.1 and n denotes total wavenumber (Lin 2009). For positive heating located at 80°E, negative and positive RWS regions are produced in southern Asia and the western North Pacific, respectively (Fig. 4a), whereas diabatic cooling at 150°E only creates one positive RWS region in the western North Pacific (Fig. 4b). Surprisingly, these two forcing anomalies generate the positive RWS approximately in the same region—that is, over the western North Pacific. It will be shown later that these two processes contribute nearly equally to the formation of the PNA-like cell (see Table 1). The total RWS can be divided into two terms: RWS generation by divergence (i.e., vortex stretching) and advection as shown in Eq. (2). Figures 4d and 4e show that the divergence term causes dipole RWSs to the north of each forcing anomaly, suggesting that this

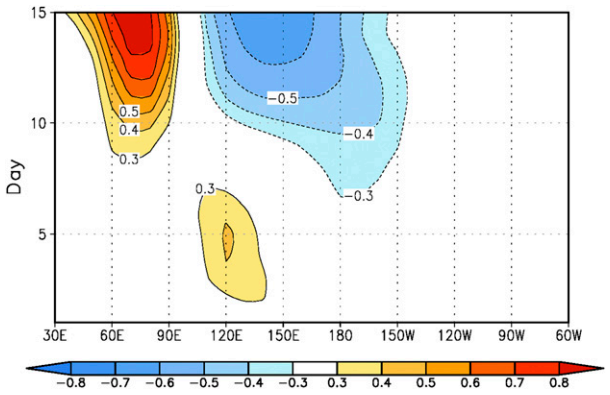

FIG. 3. Pattern correlations between the NH upper-troposphere streamfunction anomalies in response to MJO dipole forcing (Fig. 2b) and those from monopolar tropical heating forced at varying longitudes from 30°E to 60°W at 10° intervals as a function of integration time.

term is determined by the location of forcing. The advection term also shows dipole RWS regions for both enhanced (Fig. 4g) and suppressed (Fig. 4h) convection with a comparable magnitude for Indian Ocean heating (Fig. 4g), but with a considerably weak negative RWS near the central Pacific for western Pacific forcing (Fig. 4h). The positive RWS over the western North Pacific for Indian Ocean heating (Fig. 4g) is remotely formed, which will be described later. On the whole, the RWS patterns generated by advection for each individual or combined forcing (Figs. 4g–i) are very similar to those from total RWS (Figs. 4a–c). In fact, since the RWS terms related to climatological divergent wind ($-\zeta'\nabla\cdot\bar{\mathbf{v}}_\chi$ and $-\bar{\mathbf{v}}_\chi\cdot\nabla\zeta'$) are approximately one order of magnitude smaller than the other terms in Eq. (2) (not shown), the middle and bottom panels in Fig. 4 are almost identical to $-\bar{\zeta}\nabla\cdot\mathbf{v}'_\chi$ and $-\mathbf{v}'_\chi\cdot\nabla\bar{\zeta}$, respectively. The characteristics are consistent with previous results that have revealed that vorticity advection by divergent wind anomaly is predominant in developing the RWS (Sardeshmukh and Hoskins 1988; Mori and Watanabe 2008).

The RWS derived from the advection term is further separated into relative and planetary vorticity advection (Fig. 5). Again, vorticity advection by climatological divergent wind ($-\bar{\mathbf{v}}_\chi\cdot\nabla\zeta'$) is small so it is not shown. Figures 5a and 5b exhibit the RWS generated by advection of the climatological relative vorticity due to anomalous divergent wind for each forcing ($-\mathbf{v}'_\chi\cdot\nabla\bar{\xi}$, where $\bar{\xi}$ is the climatological relative vorticity). It is evident that this term (Figs. 5a and 5b) is largely responsible for the RWS generated by advection of the absolute vorticity (Figs. 4g and 4h) with a dipole pattern for 80°E forcing and a positive RWS region for 150°E forcing. In contrast, the major RWS region generated by advection of the planetary vorticity by the divergent wind anomaly ($-\beta\mathbf{v}'_\chi$) develops right near the forcing anomaly (Figs. 5c and 5d). It is of note that a weak positive RWS appearing at ~18°N over the Philippine Sea in Fig. 5c is formed by remote forcing from the Indian Ocean convection; so it seems that the planetary vorticity advection by divergent wind anomaly is also important but the effect of this positive RWS is mostly offset by the negative RWS at that location (Fig. 5a) (which is an anticyclonic climatological wind shear area to the south of the Asian–Pacific jet) induced by the relative vorticity advection due to divergent wind anomaly.

Next, the question of how the RWS develops is investigated. To elucidate the kinematic process related to relative vorticity advection, the divergent wind anomaly and the meridional gradient of the climatological relative vorticity are presented in Fig. 6. The zonal gradient of the vorticity is considerably smaller than the meridional gradient and, therefore, the former is omitted. The climatological relative vorticity exhibits the greatest meridional gradient along the jet over Asia and the Pacific in the NH. When the forcing anomaly is at 80°E (Fig. 6a), divergent flow soon arises in the upper troposphere and a southerly wind develops in the northern Indian Ocean, which is, later, bent to the right owing to the Coriolis force, eventually leading to the development of a northerly wind over the western North Pacific. Therefore, southerly wind from the northern Indian Ocean and northerly wind near the jet exit region over the western North Pacific penetrate the area with the greatest value for the meridional gradient of the climatological relative vorticity, consequently causing the negative and positive RWS regions in those regions (as shown in Fig. 5a). In case of diabatic cooling at 150°E (Fig. 6b), convergence in the upper troposphere induces northerly wind near the Asian jet exit region, leading to positive advection of the mean relative vorticity, which causes development of the positive RWS. It can be concluded that zonally asymmetric basic flow plays a role in shaping the characteristic RWS patterns depending on the location of tropical forcing. It is of interest to note that 1) a significant RWS region can be formed remotely owing to the refraction of divergent winds in the upper troposphere and 2) not only the intensity of the jet (therefore, the meridional gradient of the climatological relative vorticity) but also the zonal extent of the Asian jet seem important. The latter is important because in order to produce strong RWS due to the meridional advection of climatological relative vorticity by MJO winds, the climatological jet needs to be located to the north or northeast of the MJO convection center, from which meridional winds develop. Just as with the Indian Ocean heating anomaly, the western Pacific heating anomaly induces a dipole in

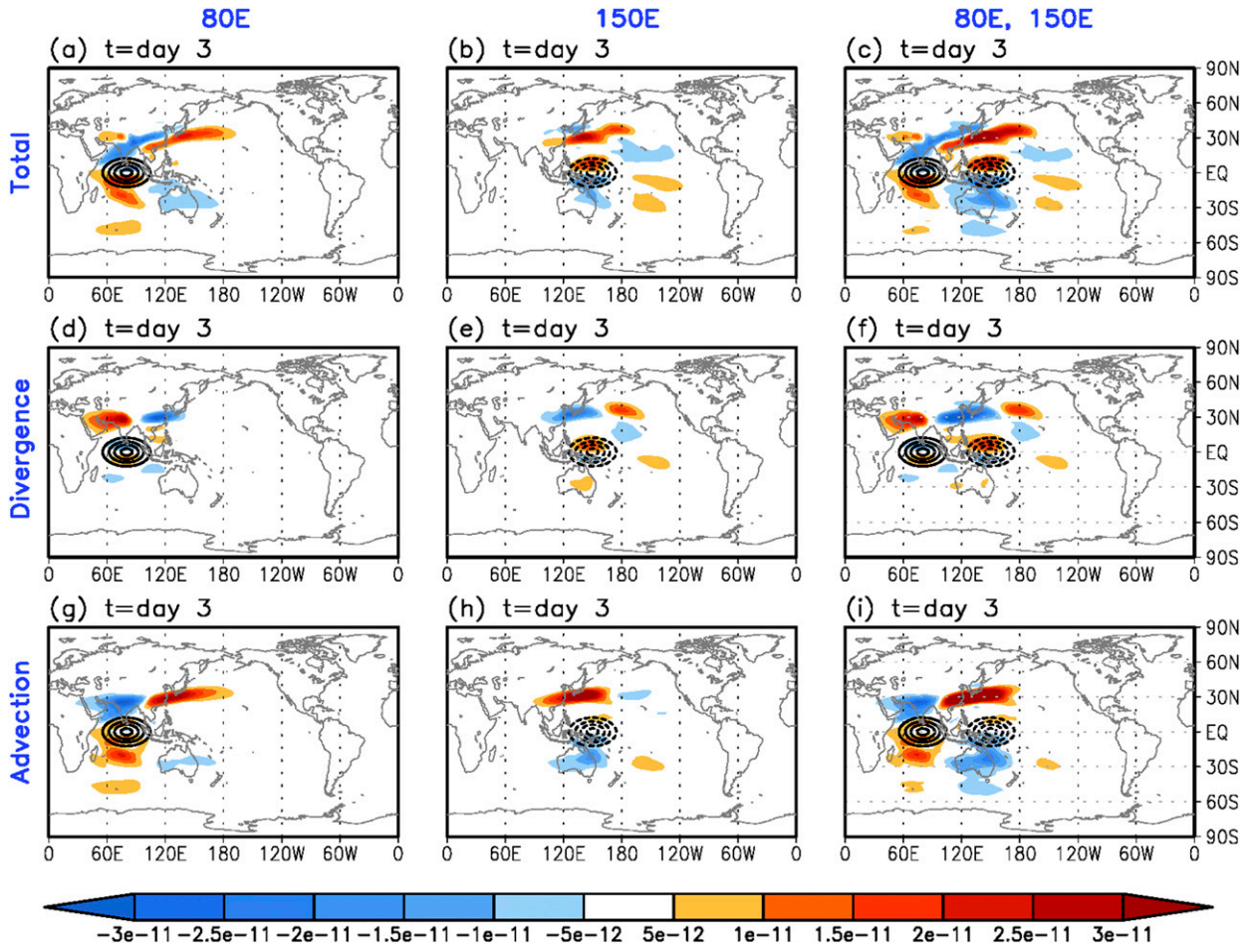

FIG. 4. Perturbation RWS at $\sigma = 0.225$ at day 3 of the model simulation for (left) diabatic heating at 80°E, (center) diabatic cooling at 150°E, and (right) dipole diabatic forcing. (a)–(c) Total RWS, (d)–(f) RWS from divergence terms, and (g)–(i) RWS from advection terms in Eq. (2). Intervals of shading are $0.5 \times 10^{-11}\,\mathrm{s}^{-2}$.

divergent wind anomalies as well, with one center to the north and another east of that one. It is just that this eastern divergent wind anomaly is not collocated with an area of strong climatological absolute vorticity gradients. Therefore, some longer-term variability (like El Niño–Southern Oscillation) can extend the Pacific jet eastward, potentially making this eastern divergent wind anomaly more important in exciting an RWS.

c. *Rossby wave seeding*

To visualize propagating barotropic Rossby waves, wave seeding and ray-tracing analysis are performed for

TABLE 1. Rossby wave penetration frequency (%) for each wavenumber. Only waves passing through at least two lobes of the PNA cells are counted. Rossby wave seeding is equally applied to each unit area in the RWS region. Note that Rossby waves that satisfy the above criteria amount to approximately 30% of all generated waves.

	Indian Ocean enhanced convection		Western Pacific suppressed convection	
Wavenumber	−RWS	+RWS	+RWS	Total
1	7.4	19.7	22.2	49.3
2	1.5	7.4	10.3	19.2
3	6.9	2.5	1.5	10.8
4	18.2	1.0	1.5	20.7
Total	34.0	30.5	35.5	100

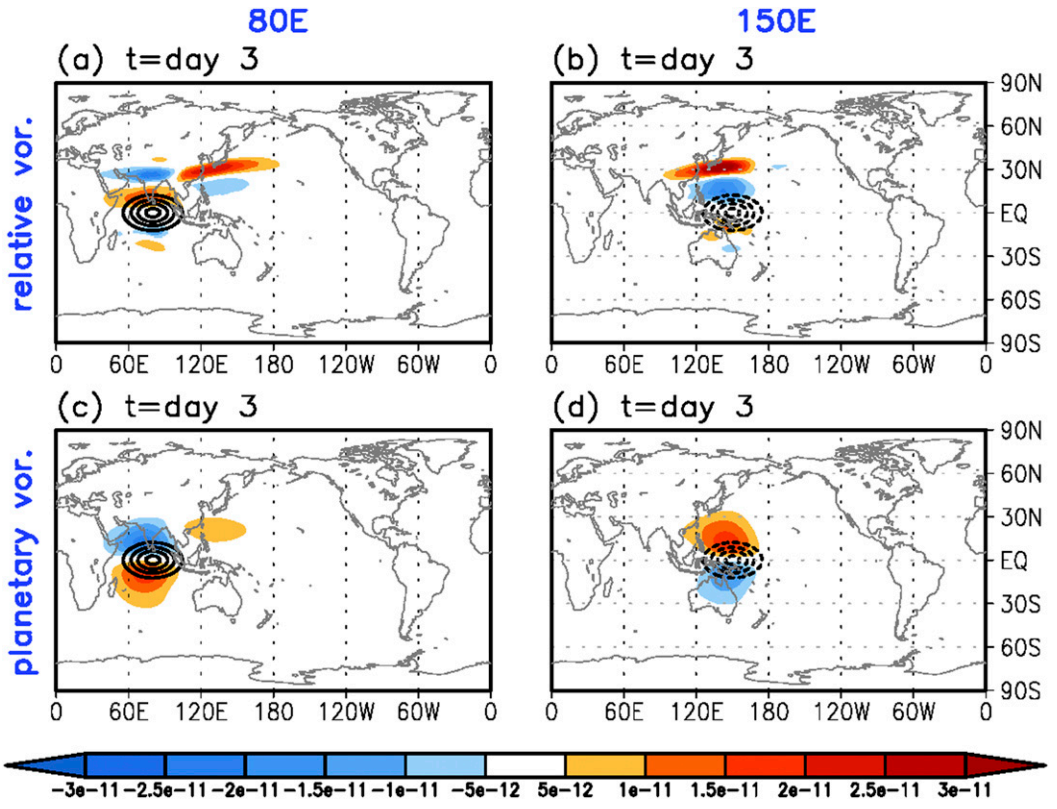

FIG. 5. As in Fig. 4, but for RWS from advection term for (left) diabatic heating at 80°E and (right) diabatic cooling at 150°E. RWS due to the advection of (a),(b) relative vorticity and (c),(d) planetary vorticity by perturbation divergent wind.

the zonal wavenumbers 1–4. Figure 7 shows the trajectory of wave activity emanating from the positive and negative RWSs for the 80°E-forcing case. It can be seen that the waves with zonal wavenumber 1 propagate northeastward toward the PNA region until they reach a turning latitude (Fig. 7a), where the sign of the meridional wavenumber changes. For the zonal wavenumber 2, some waves coming from the negative RWS near the Indian subcontinent (blue line in Fig. 7b) are directed toward the north and terminated at higher latitude,

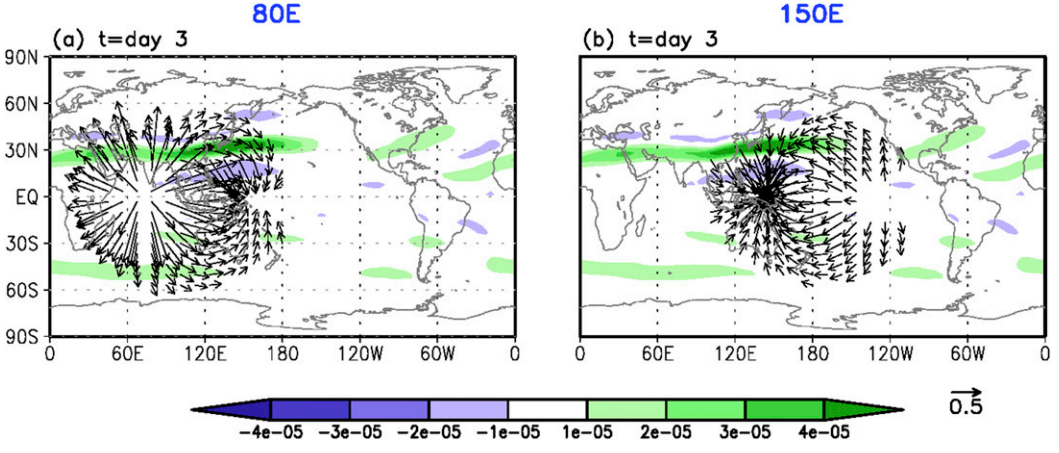

FIG. 6. Meridional gradient of the climatological relative vorticity (shaded, intervals of 1.0×10^{-5} m^{-1} s^{-1}) and perturbation divergent wind (vector, m s^{-1}) for (a) diabatic heating at 80°E and (b) diabatic cooling at 150°E at day 3 of the model integration. Wind vectors smaller than 0.2 m s^{-1} are not displayed.

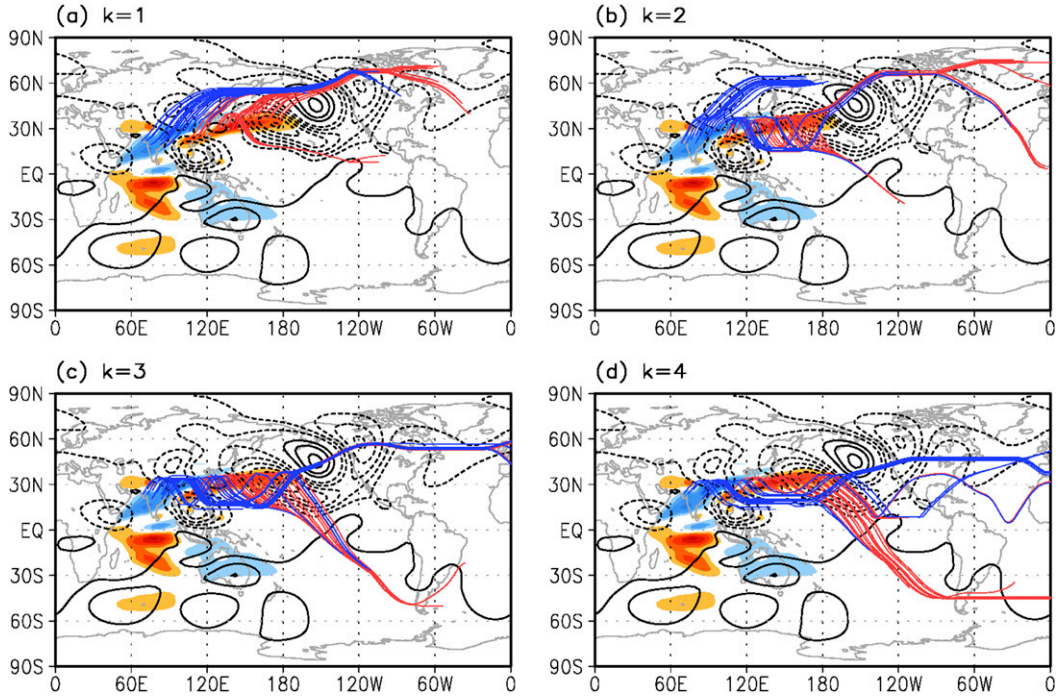

FIG. 7. Rossby wave ray path for zonal wavenumbers (a) 1, (b) 2, (c) 3, and (d) 4 for diabatic heating at 80°E. Blue (red) lines denote the ray path excited from the negative (positive) RWS in southern Asia (the western North Pacific) at day 15. Contours represent the streamfunction anomalies in response to diabatic heating at 80°E (i.e., shading in Fig. 2c). Shading is the RWS region as shown in Fig. 4a.

whereas others from the same negative source (also blue line in Fig. 7b) undulate along the subtropical Asian–Pacific jet, and then, at the jet exit, escape from the trapped region. These waves propagate first northeastward and then southward, crossing the PNA-like circulation anomaly centers. Wave undulation along the jet stream occurs because strong meridional curvature on both sides of the jet stream tends to decrease β_* (since it is $\partial f/\partial y - \partial^2\overline{U}/\partial y^2$), leading to $l = 0$. The reflection latitude on the equatorward side is located slightly to the north of the critical latitude where the mean zonal wind is zero; therefore, waves do not dissipate but are reflected toward the north. However, waves propagate slightly to the north of the circulation center over eastern North America. The waves from the positive RWS in the western North Pacific also cause the formation of the PNA-like pattern (red line in Fig. 7b) with a similar northward shifted ray for the last lobe of the PNA cells. Waves with wavenumbers 3 and 4 (Figs. 7c and 7d) penetrate the center of the last lobe over eastern North America, while some of them are reflected by the jet and caught by the critical latitude located along 15°N. The other waves that were first reflected tend to propagate southward across the equator through the tropical westerly duct (Figs. 7c and 7d). Hence, in association with Indian Ocean forcing, there are two wave source regions with three different mechanisms that may affect the downstream teleconnection anomalies: direct penetration of wave activity into the middle two lobes of the PNA cells from the negative RWS, propagation of waves once trapped inside the waveguide at the exit of the jet, and great-circle-like wave propagation from the positive RWS.

For diabatic cooling forced at 150°E, waves with zonal wavenumbers 1 and 2 also exhibit an arclike route penetrating the PNA region (Figs. 8a and 8b) and the propagating ray shows a trajectory nearly perpendicular to the principal axis of each individual anomaly cell, consistent with a quasigeostrophic Rossby wave dispersion theory. Contribution of these waves to the creation of the PNA pattern amounts to about one-third of the total wave contribution (Table 1). However, shorter waves with zonal wavenumbers 3 and 4 (Figs. 8c and 8d) do not penetrate to the higher cell in Alaska. Instead they show a more zonally oriented propagating route along lower latitudes with the ray crossing the last lobe similar to the ray in the enhanced convection at 80°E (Figs. 7c and 7d). Note that some waves of zonal wavenumber 4 propagate farther into the eastern Atlantic waveguide (Figs. 7d and 8d), along which a localized peak in stationary total wavenumber K_S exists over the Atlantic Ocean (Fig. 9c). This wave propagation feature

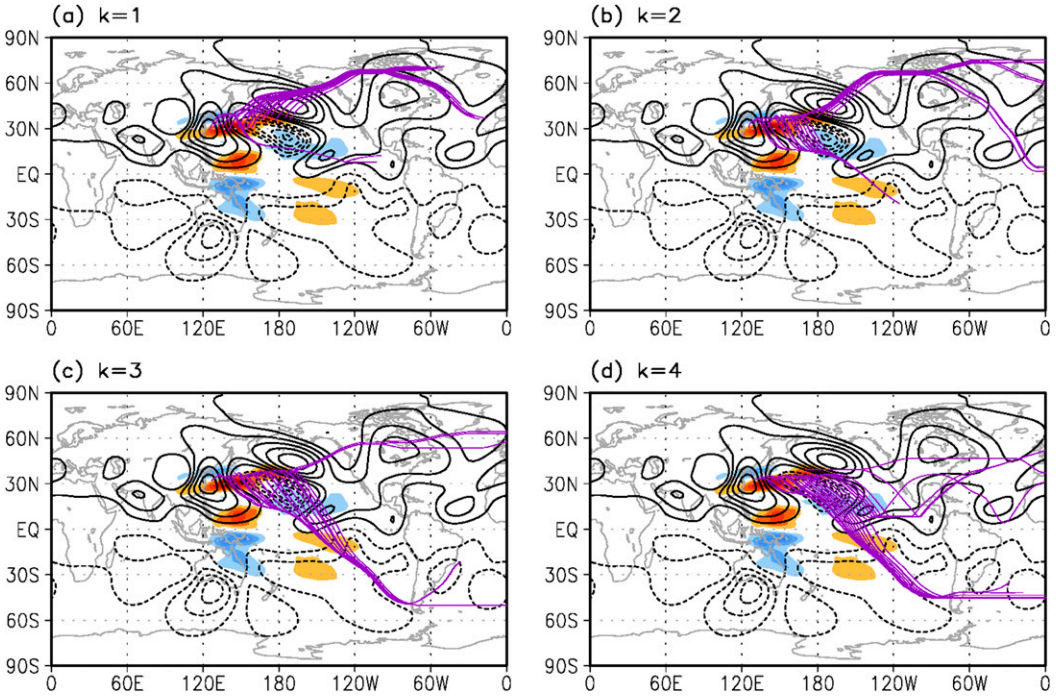

FIG. 8. As in Fig. 7, but for diabatic cooling at 150°E. Purple lines indicate the Rossby wave ray path from the positive RWS over the western North Pacific. Contours represent the streamfunction anomalies in response to diabatic cooling at 150°E (i.e., shading in Fig. 2d). Shading is the RWS region as shown in Fig. 4b.

has been reported by Seo et al. (2016), who demonstrated that the waves with zonal wavenumber 4 can result in significant surface air temperature variations over eastern Europe.

In general, the above results are in agreement with the Rossby wave theory, in which waves tend to refract toward the region with higher values of K_S, as shown in Fig. 9c (Hoskins and Ambrizzi 1993). The wave reflects at a turning latitude where the meridional wavenumber l is zero or the meridional gradient of absolute vorticity β_* is small (Fig. 9b) and is absorbed at a critical latitude where the background zonal wind $\overline{U}$ is zero (Fig. 9a). The Rossby wave penetration frequency is summarized in Table 1, where only waves passing through at least two lobes of the PNA cells are counted. Interestingly, the three RWS regions represent nearly equal contributions and Indian Ocean forcing produces double the wave penetration frequency compared to western Pacific forcing, indicating that far upstream forcing over the Indian Ocean plays a crucial role in creating the PNA-like pattern.

d. *Energetic transformation from divergent flow to rotational flow*

Chen and Wiin-Nielsen (1976) have identified a transformation of divergent kinetic energy to rotational kinetic energy in the large-scale atmospheric circulation. For our situation, this implies that the divergent flow initiated by external forcing (Chen et al. 1978; Buechler and Fuelberg 1986) plays a catalytic role in the conversion from potential energy to rotational kinetic energy. To examine this energy conversion, the ratio of divergent kinetic energy or rotational kinetic energy to the total kinetic energy is calculated (not shown) using our model experiment forced by tropical dipole convective anomalies at 80° and 150°E. Until day 2 or 3, divergent kinetic energy occupies a larger part of the kinetic energy than rotational kinetic energy. Rotational kinetic energy explains most of the kinetic energy after day 4, indicating that potential energy is first converted to divergent kinetic energy and then rotational kinetic energy. Therefore, the RWS, which is created by divergent flow, acts as a route for the energy conversion from potential energy to rotational kinetic energy.

This argument can also be confirmed by calculating spatial patterns of the RWS and Rossby wave propagation (RWP) comprising the vorticity tendency equation along the integration time. In the vorticity budget equation, the vorticity tendency is balanced with divergent flow part (i.e., RWS), rotational flow part [i.e., RWP; the second and third terms in Eq. (1)], and residual (i.e., vertical advection and twisting) terms. These three terms are all directly calculated from the model output. To see which component among the three

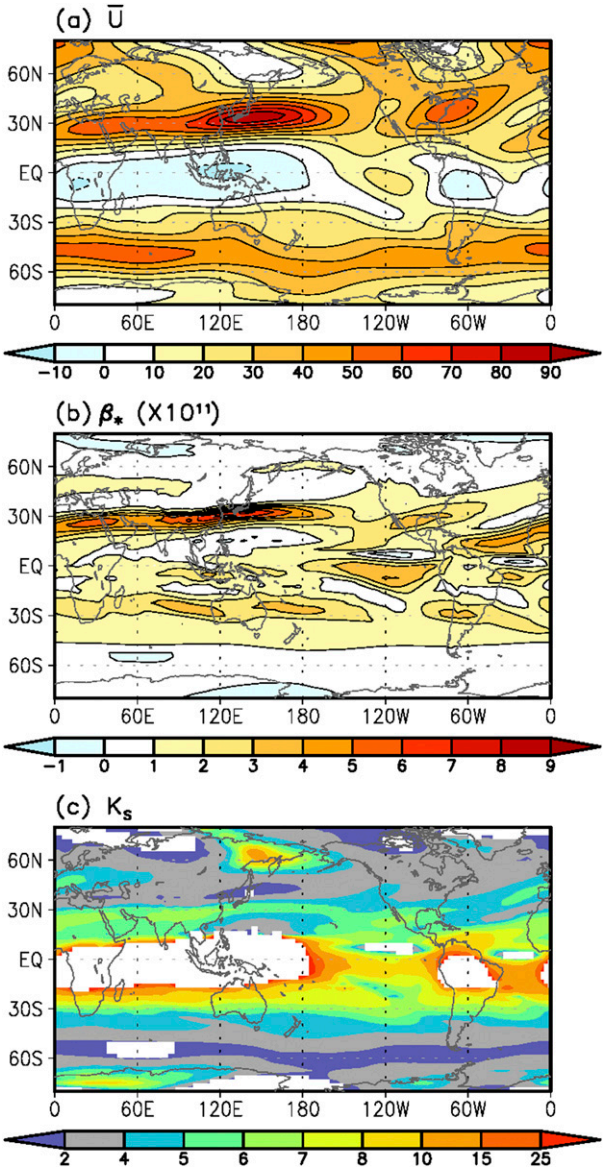

FIG. 9. (a) Climatological DJF 200-hPa zonal wind $\overline{U}$ (intervals of 10 m s^{-1}) and (b) the meridional gradient of the absolute vorticity β_* at the Mercator coordinate (intervals of 1.0×10^{-11} m^{-1} s^{-1}). (c) Stationary total wavenumber K_S represented by contours at zonal wavenumbers 2, 4, 5, 6, 7, 8, 10, 15, and 25. Singular values of K_S, which occur for the negative value of β_* or $\overline{U}$, are not displayed.

balancing terms (RWS, RWP, and residual) is dominant in the evolving circulation response, pattern correlation between the vorticity tendency and its three components is calculated (Fig. 10). It can be seen that after diabatic forcing is turned on, the RWS has the highest pattern correlation until day 3 and decays afterward, whereas the RWP gradually develops and shows the highest pattern correlation among the three components after

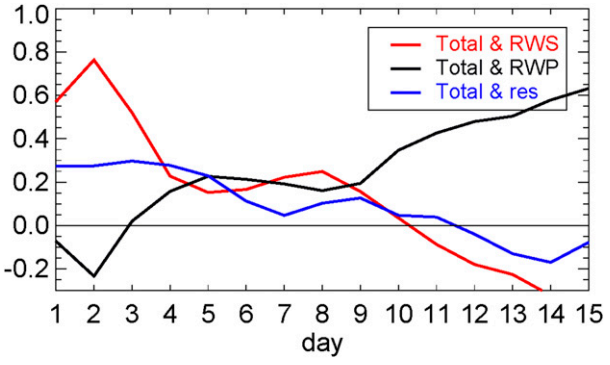

FIG. 10. Pattern correlation coefficients between the vorticity tendency and the three balance terms (i.e., the RWS, RWP, and residual) at $\sigma = 0.225$ for the NH as a function of integration day.

day 9. The residual term is important only during transition period between days 4 and 5. This is in contrast to a previous study (Kim et al. 2006), which argued that vertical motion arising by quasigeostrophic balance near the jet stream entrance and the tilting of vorticity are important and therefore these terms can be a source of the midlatitude teleconnection of the MJO. Our analysis evidently indicates energy conversion from divergent flow to rotational flow, or equivalently, the sequential transition of the RWS to the RWP. In fact, the conversion from divergent kinetic energy to rotational kinetic flow is very fast with a time scale of 3 or 4 days.

e. Capability of the PNA pattern generation in response to the MJO in climate models

Recently, using 27 different climate simulations participating in the WGNE (MJO-TF)/GASS MJO global model comparison project, Jiang et al. (2015) have identified the eight good and six poor MJO-simulating models. To verify whether a well-performing model produces a better circulation response in the PNA region, we present a composite map of the upper-level streamfunction anomalies at several lag days for the initial MJO phase 2 in Fig. 11. The circulation anomalies in the good model composite (Figs. 11a–c) resemble the observation (Fig. 1) over the PNA region much more closely than those in poor model composite (Figs. 11d–f). Pattern correlations of the good model composite reach as high as 0.8–0.9, whereas those for the poor model are only 0.1–0.3. In fact, the fidelity in simulating the entire global circulation pattern is much higher for the good model composite. At all lag days, the poor model composite (Figs. 11d–f) does not show any of the four circulation anomalies related to the PNA-like circulation pattern. This is caused by the poor simulation of MJO convection in the poor models (e.g., monopole-like convection, incorrect position of the convection,

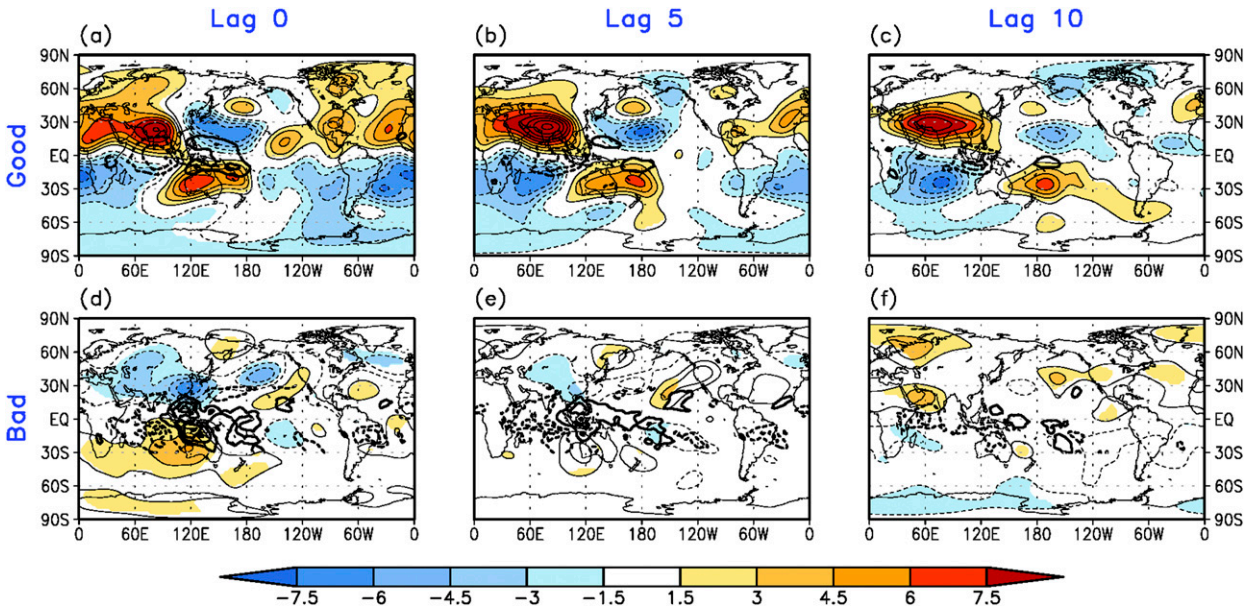

FIG. 11. As in Fig. 1, except for (a)–(c) the good MJO simulation model and (d)–(f) the poor MJO simulation model. The intervals of model streamfunction (shaded) and OLR (thick solid and dotted lines) are $1.5 \times 10^6\,\mathrm{m^2\,s^{-1}}$ and $10\,\mathrm{W\,m^{-2}}$, respectively.

and less-organized convection anomalies; Kim and Seo 2017). Since the global circulation response is known to be extremely dependent upon the performance of the MJO simulation (Seo and Wang 2010), it is evident that the good MJO simulation models are able to reproduce the circulation anomalies well. This result has an important ramification on weather forecasts over the PNA region, because the MJO itself can be predictable 15–25 days earlier in high-performing climate models (e.g., Seo et al. 2009; Gottschalck et al. 2010; Vitart and Molteni 2010). Since Rossby wave propagation from the tropical MJO to the PNA region takes 1–2 weeks, skillful prediction of the PNA pattern can be achieved with a 1-month time scale. In a more practical application of this information, Seo et al. (2016) demonstrated the physical mechanisms responsible for surface air temperature variations over the PNA region in relation to MJO forcing.

4. Discussion and conclusions

The MJO triggers a PNA-like pattern on intraseasonal time scales. Since the PNA is a predominant mode in the extratropics and provides a source of predictability, the dynamical mechanism of its formation should be investigated in detail to improve weather and climate prediction skills in this region. In this study, the linear response of the NH upper-tropospheric circulation anomaly to MJO convective forcing is examined using a dry GCM and barotropic Rossby wave theory. Specifically, the formation mechanisms of the negative PNA-like teleconnection pattern in response to the MJO phase 2, where enhanced convection is located over the Indian Ocean and suppressed convection is situated over the western Pacific are investigated. A two-step process characterized by the sequential development of a Rossby wave source (RWS), followed by Rossby wave propagation (RWP) can explain much of the dynamical mechanisms responsible for the formation of this pattern. In addition, the conventional Rossby wave theory is demonstrated to be valid. The process for the formation of a positive PNA-like pattern induced at MJO phase 6 is identical, although with a reversed sign.

Model simulation shows that both forcing anomalies contribute to creating the PNA-like pattern. First, Indian Ocean forcing induces two major RWS regions: a negative region around southern Asia, including the Indian subcontinent, and a positive region over the western North Pacific (WNP) (Fig. 12a). Formation of the negative RWS to the north of the area of enhanced forcing in the Indian Ocean is easy to understand (i.e., through southerly MJO divergent wind crossing the Asian jet). However, formation of the WNP RWS is unexpected since it is located far downstream of the forcing region. Ultimately, this RWS is formed by refracted northerly divergent wind due to the Coriolis force crossing the jet stream (Fig. 12a). The relevant major dynamical process is advection of a climatological relative vorticity by the divergent wind anomaly. Another interesting result is that Rossby wave propagation

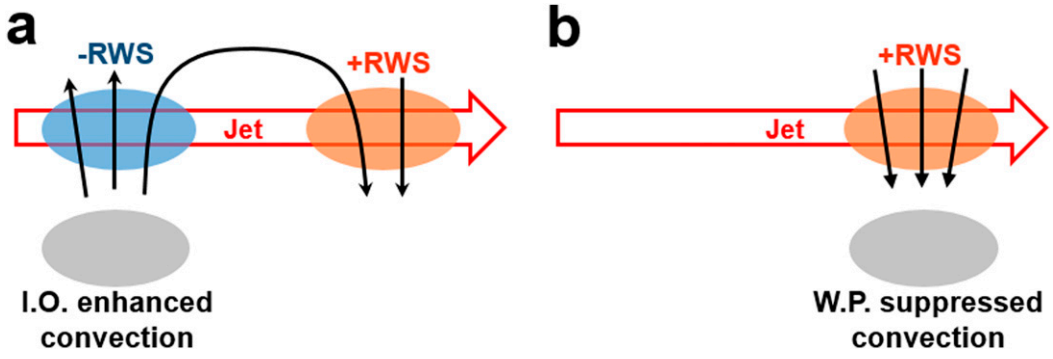

FIG. 12. Schematic diagram illustrating RWS formation mechanisms in response to tropical (a) Indian Ocean heating and (b) western Pacific cooling. Vector represents upper-level perturbation divergent wind excited by tropical forcing. The Asian jet is denoted by the red arrow. Positive (negative) RWS region is shaded as orange (blue).

to the PNA region from the RWS formed by Indian Ocean forcing occurs in three ways: 1) a direct arclike propagation driven by the longest waves (i.e., zonal wavenumber 1) occurs from the negative RWS to the PNA region, which normally affects the second and third lobes of the PNA cells: the circulation anomalies over the midlatitude North Pacific and Alaska (Fig. 13a), 2) waves shorter than the above are first displaced downstream by the waveguide effect and then emanated at the jet exit to the PNA region (Fig. 13a), and 3) waves with zonal wavenumbers 1 and 2 exhibit a canonical Rossby wave propagation from the positive RWS at the jet exit to the PNA region (Fig. 13b).

On the other hand, the positive RWS induced by western Pacific forcing (Fig. 12b) shows similar characteristics to feature 3 stated above (Fig. 13c), with some relaxation in that much shorter waves also contribute to the formation of the southern cells (Figs. 8c and 8d). All four propagation mechanisms are shown in Fig. 13, where it is seen that both enhanced and suppressed convective forcing anomalies contribute to the formation of the PNA-like pattern and its reinforcement. As shown in Fig. 12 or 13, it is of special interest to notice that the zonal extent of the Asian–Pacific jet is similar to the propagation range of MJO convection. So, convective forcing at any location in the warm pool has a high possibility to generate an RWS region and resultant downstream circulation anomalies. It is also proposed that the most effective way of generating a PNA-like teleconnection pattern is creation of an RWS region at the exit of the jet. Thus, MJO phases 2 and 3 (6 and 7) are a strong candidate for PNA-like pattern formation since significant tropical suppressed (enhanced) convection at these phases is situated to the south of the jet exit. Of course, upstream diabatic forcing also helps develop an RWS region at this location as mentioned above. If the jet is assumed to be retracted toward the west, MJO meridional wind coming from convective forcing at 150°E (or from farther east) will show little interaction with the background relative vorticity appearing along the jet; so a significant RWS will not

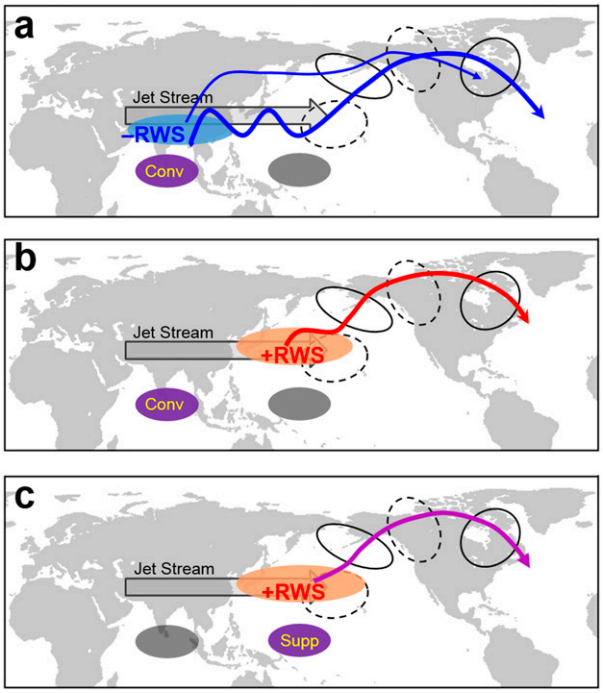

FIG. 13. Schematic diagram illustrating PNA formation mechanisms in response to the MJO. Wave propagation (colored lines) for tropical (a),(b) Indian Ocean heating and (c) western Pacific cooling. Rossby wave ray emanated from the (a) negative (blue shading) and (b) positive (orange shading) RWS due to forcing over the tropical Indian Ocean. Two routes (thin and thick blue lines) reach the PNA region in (a). Rossby wave ray (purple line) emanated from the positive RWS (orange) due to forcing over the western Pacific is seen in (c). Notice that there are a total of four different ways of wave propagation into the PNA regions.

develop and the circulation pattern over the PNA region will not be well organized.

The energy transformations taking place during the development of circulation anomalies over the PNA region are rather clear. Potential energy arising from diabatic forcing (in the temperature equation) first generates divergent flow and increases divergent kinetic energy, developing an RWS region. Through the RWS, this energy is converted to rotational kinetic energy (in the form of circulation cells).

This study revealed that background mean flow is also important for establishing the RWS pattern. Since the background flow would change in the future under conditions of global warming, it is anticipated that the location of the major RWS region and therefore the teleconnection pattern would also change. For example, a number of studies (e.g., Hu et al. 2000; Yin 2005; Lorenz and DeWeaver 2007) reported that the jet stream over the North Pacific will shift poleward under future climate scenarios. Therefore, future teleconnection pattern deserves further investigation.

Acknowledgments. The authors thank Dr. Seok-Woo Son and two anonymous reviewers for their helpful and constructive comments, which greatly improved the manuscript. This work was supported by the National Research Foundation of Korea (NRF) grants funded by the Korean government (MSIP) NRF-2015R1A2A2A01006663 and the Korea Meteorological Administration Research and Development Program under Grant KMIPA 2015–2113. The authors would like to acknowledge the support from the Korea Institute of Science and Technology Information (KISTI).

REFERENCES

Branstator, G., 1990: Low-frequency patterns induced by stationary waves. *J. Atmos. Sci.*, **47**, 629–648, doi:10.1175/1520-0469(1990)047<0629:LFPIBS>2.0.CO;2.

——, 1992: The maintenance of low-frequency atmospheric anomalies. *J. Atmos. Sci.*, **49**, 1924–1945, doi:10.1175/1520-0469(1992)049<1924:TMOLFA>2.0.CO;2.

Buechler, D. E., and H. E. Fuelberg, 1986: Budgets of divergent and rotational kinetic energy during two periods of intense convection. *Mon. Wea. Rev.*, **114**, 95–114, doi:10.1175/1520-0493(1986)114<0095:BODARK>2.0.CO;2.

Cash, B., and S. Lee, 2001: Observed nonmodal growth of the Pacific–North American teleconnection pattern. *J. Climate*, **14**, 1017–1028, doi:10.1175/1520-0442(2001)014<1017:ONGOTP>2.0.CO;2.

Chen, T.-C., and A. Wiin-Nielsen, 1976: On the kinetic energy of the divergent and nondivergent flow in the atmosphere. *Tellus*, **28A**, 486–498, doi:10.1111/j.2153-3490.1976.tb00697.x.

——, J. C. Alpert, and T. W. Schlatter, 1978: The effects of divergent and nondivergent winds on the kinetic energy budget of a mid-latitude cyclone: A case study. *Mon. Wea. Rev.*, **106**, 458–468, doi:10.1175/1520-0493(1978)106<0458:TEODAN>2.0.CO;2.

Dee, D., and Coauthors, 2011: The ERA-Interim reanalysis: Configuration and performance of the data assimilation system. *Quart. J. Roy. Meteor. Soc.*, **137**, 553–597, doi:10.1002/qj.828.

Feldstein, S., 2002: Fundamental mechanisms of the growth and decay of the PNA teleconnection pattern. *Quart. J. Roy. Meteor. Soc.*, **128**, 775–796, doi:10.1256/0035900021643683.

Franzke, C., and S. B. Feldstein, 2005: The continuum and dynamics of Northern Hemisphere teleconnection patterns. *J. Atmos. Sci.*, **62**, 3250–3267, doi:10.1175/JAS3536.1.

——, ——, and S. Lee, 2011: Synoptic analysis of the Pacific–North American teleconnection pattern. *Quart. J. Roy. Meteor. Soc.*, **137**, 329–346, doi:10.1002/qj.768.

Gordon, C. T., and W. F. Stern, 1982: A description of the GFDL global spectral model. *Mon. Wea. Rev.*, **110**, 625–644, doi:10.1175/1520-0493(1982)110<0625:ADOTGG>2.0.CO;2.

Goss, M., and S. B. Feldstein, 2015: The impact of the initial flow on the extratropical response to Madden–Julian oscillation convective heating. *Mon. Wea. Rev.*, **143**, 1104–1121, doi:10.1175/MWR-D-14-00141.1.

Gottschalck, J., and Coauthors, 2010: A framework for assessing operational model Madden–Julian oscillation forecasts: A CLIVAR MJO working group project. *Bull. Amer. Meteor. Soc.*, **91**, 1247–1258, doi:10.1175/2010BAMS2816.1.

Hoskins, B. J., and D. J. Karoly, 1981: The steady linear response of a spherical atmosphere to thermal and orographic forcing. *J. Atmos. Sci.*, **38**, 1179–1196, doi:10.1175/1520-0469(1981)038<1179:TSLROA>2.0.CO;2.

——, and T. Ambrizzi, 1993: Rossby wave propagation on a realistic longitudinally varying flow. *J. Atmos. Sci.*, **50**, 1661–1671, doi:10.1175/1520-0469(1993)050<1661:RWPOAR>2.0.CO;2.

Hu, Z.-Z., L. Bengtsson, and K. Arpe, 2000: Impact of global warming on the Asian winter monsoon in a coupled GCM. *J. Geophys. Res.*, **105**, 4607–4624, doi:10.1029/1999JD901031.

Jeong, J.-H., B.-M. Kim, C.-H. Ho, and Y.-H. Noh, 2008: Systematic variation in wintertime precipitation in East Asia by MJO-induced extratropical vertical motion. *J. Climate*, **21**, 788–801, doi:10.1175/2007JCLI1801.1.

Jiang, X., and Coauthors, 2015: Vertical structure and physical processes of the Madden-Julian oscillation: Exploring key model physics in climate simulations. *J. Geophys. Res. Atmos.*, **120**, 4718–4748, doi:10.1002/2014JD022375.

Jin, F.-F., and B. J. Hoskins, 1995: The direct response to tropical heating in a baroclinic atmosphere. *J. Atmos. Sci.*, **52**, 307–319, doi:10.1175/1520-0469(1995)052<0307:TDRTTH>2.0.CO;2.

——, L.-L. Pan, and M. Watanabe, 2006a: Dynamics of synoptic eddy and low-frequency flow interaction. Part I: A linear closure. *J. Atmos. Sci.*, **63**, 1677–1694, doi:10.1175/JAS3715.1.

——, ——, and ——, 2006b: Dynamics of synoptic eddy and low-frequency flow interaction. Part II: A theory for low-frequency modes. *J. Atmos. Sci.*, **63**, 1695–1708, doi:10.1175/JAS3716.1.

Kim, B.-M., G.-H. Lim, and K.-Y. Kim, 2006: A new look at the midlatitude–MJO teleconnection in the northern hemisphere winter. *Quart. J. Roy. Meteor. Soc.*, **132**, 485–503, doi:10.1256/qj.04.87.

Kim, G.-U., and K.-H. Seo, 2017: Identifying a key physical factor sensitive to the performance of Madden–Julian oscillation simulation in climate models. *Climate Dyn.*, doi:10.1007/s00382-017-3616-y, in press.

Kug, J.-S., and F.-F. Jin, 2009: Left-hand rule for synoptic eddy feedback on low-frequency flow. *Geophys. Res. Lett.*, **36**, L05709, doi:10.1029/2008GL036435.

Lau, N.-C., 1988: Variability of the observed midlatitude storm tracks in relation to low-frequency changes in the circulation pattern. *J. Atmos. Sci.*, **45**, 2718–2743, doi:10.1175/1520-0469(1988)045<2718:VOTOMS>2.0.CO;2.

Liebmann, B., and C. A. Smith, 1996: Description of a complete (interpolated) outgoing longwave radiation dataset. *Bull. Amer. Meteor. Soc.*, **77**, 1275–1277.

Lin, H., 2009: Global extratropical response to diabatic heating variability of the Asian summer monsoon. *J. Atmos. Sci.*, **66**, 2697–2713, doi:10.1175/2009JAS3008.1.

——, and G. Brunet, 2009: The influence of the Madden–Julian oscillation on Canadian wintertime surface air temperature. *Mon. Wea. Rev.*, **137**, 2250–2262, doi:10.1175/2009MWR2831.1.

——, ——, and R. Mo, 2010: Impact of the Madden–Julian oscillation on wintertime precipitation in Canada. *Mon. Wea. Rev.*, **138**, 3822–3839, doi:10.1175/2010MWR3363.1.

Lorenz, D. J., and E. T. DeWeaver, 2007: Tropopause height and the zonal wind response to global warming in the IPCC scenario integrations. *J. Geophys. Res.*, **112**, D10119, doi:10.1029/2006JD008087.

Madden, R. A., and P. R. Julian, 1972: Description of global-scale circulation cells in the tropics with a 40–50 day period. *J. Atmos. Sci.*, **29**, 1109–1123, doi:10.1175/1520-0469(1972)029<1109:DOGSCC>2.0.CO;2.

Matthews, A. J., B. J. Hoskins, and M. Masutani, 2004: The global response to tropical heating in the Madden-Julian oscillation during the northern winter. *Quart. J. Roy. Meteor. Soc.*, **130**, 1991–2011, doi:10.1256/qj.02.123.

Mori, M., and M. Watanabe, 2008: The growth and triggering mechanisms of the PNA: A MJO-PNA coherence. *J. Meteor. Soc. Japan*, **86**, 213–236, doi:10.2151/jmsj.86.213.

Nakamura, H., and J. M. Wallace, 1993: Synoptic behavior of baroclinic eddies during the blocking onset. *Mon. Wea. Rev.*, **121**, 1892–1903, doi:10.1175/1520-0493(1993)121<1892:SBOBED>2.0.CO;2.

Press, W. H., S. A. Teukolsky, W. Y. Vetterling, and B. P. Flannery, 1992: *Numerical Recipes in Fortran 77: The Art of Scientific Computing.* Cambridge University Press, 931 pp.

Ren, H.-L., F.-F. Jin, J.-S. Kug, J.-X. Zhao, and J. Park, 2009: A kinematic mechanism for positive feedback between synoptic eddies and NAO. *Geophys. Res. Lett.*, **36**, L11709, doi:10.1029/2009GL037294.

Sardeshmukh, P. D., and B. J. Hoskins, 1984: Spatial smoothing on the sphere. *Mon. Wea. Rev.*, **112**, 2524–2529, doi:10.1175/1520-0493(1984)112<2524:SSOTS>2.0.CO;2.

——, and ——, 1988: The generation of global rotational flow by steady idealized tropical divergence. *J. Atmos. Sci.*, **45**, 1228–1251, doi:10.1175/1520-0469(1988)045<1228:TGOGRF>2.0.CO;2.

Seo, K.-H., and W. Wang, 2010: The Madden–Julian oscillation simulated in the NCEP Climate Forecast System model: The importance of stratiform heating. *J. Climate*, **23**, 4770–4793, doi:10.1175/2010JCLI2983.1.

——, and S.-W. Son, 2012: The global atmospheric circulation response to tropical diabatic heating associated with the Madden–Julian oscillation during northern winter. *J. Atmos. Sci.*, **69**, 79–96, doi:10.1175/2011JAS3686.1.

——, W. Wang, J. Gottschalck, Q. Zhang, J.-K. E. Schemm, W. R. Higgins, and A. Kumar, 2009: Evaluation of MJO forecast skill from several statistical and dynamical forecast models. *J. Climate*, **22**, 2372–2388, doi:10.1175/2008JCLI2421.1.

——, H.-J. Lee, and D. M. W. Frierson, 2016: Unraveling the teleconnection mechanisms that induce wintertime temperature anomalies over the Northern Hemisphere continents in response to the MJO. *J. Atmos. Sci.*, **73**, 3557–3571, doi:10.1175/JAS-D-16-0036.1.

Simmons, A. J., J. M. Wallace, and G. W. Branstator, 1983: Barotropic wave propagation and instability, and atmospheric teleconnection patterns. *J. Atmos. Sci.*, **40**, 1363–1392, doi:10.1175/1520-0469(1983)040<1363:BWPAIA>2.0.CO;2.

Vecchi, G. A., and N. A. Bond, 2004: The Madden-Julian Oscillation (MJO) and northern high latitude wintertime surface air temperatures. *Geophys. Res. Lett.*, **31**, L04104, doi:10.1029/2003GL018645.

Vitart, F., and F. Molteni, 2010: Simulation of the Madden–Julian Oscillation and its teleconnections in the ECMWF forecast system. *Quart. J. Roy. Meteor. Soc.*, **136**, 842–855, doi:10.1002/qj.623.

Wallace, J. M., and D. S. Gutzler, 1981: Teleconnections in the geopotential height field during the Northern Hemisphere winter. *Mon. Wea. Rev.*, **109**, 784–804, doi:10.1175/1520-0493(1981)109<0784:TITGHF>2.0.CO;2.

Wheeler, M. C., and H. H. Hendon, 2004: An all-season real-time multivariate MJO index: Development of an index for monitoring and prediction. *Mon. Wea. Rev.*, **132**, 1917–1932, doi:10.1175/1520-0493(2004)132<1917:AARMMI>2.0.CO;2.

Yin, J. H., 2005: A consistent poleward shift of the storm tracks in simulations of 21st century climate. *Geophys. Res. Lett.*, **32**, L18701, doi:10.1029/2005GL023684.

Yoo, C., S. Lee, and S. Feldstein, 2012: Mechanisms of Arctic surface air temperature change in response to the Madden–Julian oscillation. *J. Climate*, **25**, 5777–5790, doi:10.1175/JCLI-D-11-00566.1.

Zhou, F., H.-L. Ren, X.-F. Xu, and Y. Zhou, 2017: Understanding positive feedback between PNA and synoptic eddies by eddy structure decomposition method. *Climate Dyn.*, doi:10.1007/s00382-016-3304-3, in press.

Zhou, S., M. L'Heureux, S. Weaver, and A. Kumar, 2012: A composite study of the MJO influence on the surface air temperature and precipitation over the continental United States. *Climate Dyn.*, **38**, 1459–1471, doi:10.1007/s00382-011-1001-9.